

## THE COSMIC-RAY ANTIPROTON FLUX BETWEEN 0.62 AND 3.19 GeV MEASURED NEAR SOLAR MINIMUM ACTIVITY

M. BOEZIO,<sup>1</sup> P. CARLSON, T. FRANCKE, AND N. WEBER  
Royal Institute of Technology (KTH), S-104 05 Stockholm, Sweden

M. SUFFERT  
Centre des Recherches Nucléaires, BP20, F-67037 Strasbourg-Cedex, France

M. HOF, W. MENN, AND M. SIMON  
Universität Siegen, 57068 Siegen, Germany

S. A. STEPHENS  
Tata Institute of Fundamental Research, Bombay 400 005, India

R. BELLOTTI, F. CAFAGNA, M. CASTELLANO, M. CIRCELLA, G. DE CATALDO, C. DE MARZO,  
N. GIGLIETTO, AND P. SPINELLI  
Dipartimento di Fisica dell'Università and Sezione INFN di Bari, Via Amendola 173, I-70126 Bari, Italy

M. BOCCIOLINI, P. PAPINI, A. PEREGO, S. PICCARDI, AND P. SPILLANTINI  
Dipartimento di Fisica dell'Università and Sezione INFN di Firenze, Largo Enrico Fermi 2, I-50125 Firenze, Italy

G. BASINI AND M. RICCI  
Laboratori Nazionali INFN, Via Enrico Fermi 40, CP 13, I-00044 Frascati, Italy

A. CODINO, N. FINETTI, AND C. GRIMANI  
Dipartimento di Fisica dell'Università and Sezione INFN di Perugia, Via Pascoli, I-06100 Perugia, Italy

M. CANDUSSO, M. CASOLINO, M. P. DE PASCALE, A. MORSELLI, P. PICOZZA, AND R. SPARVOLI  
Dipartimento di Fisica dell'Università and Sezione INFN di Roma, Tor Vergata, Via della Ricerca Scientifica 1, I-00133 Roma, Italy

G. BARBIELLINI, U. BRAVAR, P. SCHIAVON, A. VACCHI, AND N. ZAMPA  
Dipartimento di Fisica dell'Università and Sezione INFN di Trieste, Via A. Valerio 2, I-34147 Trieste, Italy

J. W. MITCHELL, J. F. ORMES, AND R. E. STREITMATTER  
Code 661, NASA/Goddard Space Flight Center, Greenbelt, MD 20771

AND

R. L. GOLDEN<sup>2</sup> AND S. J. STOCHAJ  
Box 3-PAL, New Mexico State University, Las Cruces, NM 88003

Received 1997 January 15; accepted 1997 April 23

### ABSTRACT

We report on the absolute antiproton flux and the antiproton to proton ratio in the energy range 0.62–3.19 GeV at the top of the atmosphere, measured by the balloon-borne experiment CAPRICE flown from Lynn Lake, Manitoba, Canada, on 1994 August 8–9. The experiment used the New Mexico State University WiZard/CAPRICE balloon-borne magnet spectrometer equipped with a solid radiator Ring Imaging Cherenkov (RICH) detector and a silicon-tungsten calorimeter for particle identification. This is the first time a RICH is used together with an imaging calorimeter in a balloon experiment, and it allows antiprotons to be clearly identified over the rigidity range 1.2–4 GV. Nine antiprotons were identified in the energy range 0.62–3.19 GeV at the top of the atmosphere. The data were collected over 18 hr at a mean residual atmosphere of 3.9 g cm<sup>-2</sup>. The absolute antiproton flux is consistent with a pure secondary production of antiprotons during the propagation of cosmic rays in the Galaxy.

*Subject headings:* balloons — cosmic rays — elementary particles — Sun: activity

### 1. INTRODUCTION

Antimatter in the form of antiprotons and positrons is a natural component of cosmic rays being produced in the interaction between cosmic-ray nuclei and the interstellar medium. Detailed knowledge of the antimatter flux is important in order to fully understand the origin, production, and the transport mechanisms of cosmic rays in our Galaxy. The first experimental evidence for the presence of antiprotons in cosmic rays was reported by Golden et al. (1979) and was subsequently followed by other experiments (Bogomolov et al. 1979; Buffington, Schindler, & Penny-

packer 1981), which all report a ratio of the flux of antiprotons to protons above that expected for a purely secondary production process.

Subsequently, several ideas were suggested to explain the antiproton excess: antimatter reaching our Galaxy from antimatter galaxies in a baryon-antibaryon symmetric universe (e.g., Stecker, Protheroe, & Kazanas 1981; Stecker & Wolfendale 1984), antimatter production by dark matter annihilation, and antimatter production by the evaporation of primordial mini-black holes (e.g., Silk & Srednicki 1984; Rudaz & Stecker 1988; Kiraly, Wdowczyk, & Wolfendale 1981). A particular feature of secondary antiproton production in proton-proton collisions is the kinematics of the reaction that result in a production threshold. A proton flux of the form  $dn/dE = A \times E^{-2.7}$ , where  $E$  is the proton

<sup>1</sup> Also at Sezione INFN di Trieste, Via A. Valerio 2, I-34147 Trieste, Italy

<sup>2</sup> Deceased.

kinetic energy and  $n$  is the number of protons per unit time, solid angle, and energy, will produce a ratio that increases rapidly as a function of energy  $E$  up to about 5 GeV.

Meanwhile, a number of experiments were performed in the energy range starting at a few hundred MeV up to about 3 GeV that confirmed the secondary antiproton production hypothesis (Stochaj et al. 1990; Salamon et al. 1990; Mitchell et al. 1996; Moiseev et al. 1997). The major difficulty in measuring the antimatter flux is the positive identification of the rare antimatter particles in the presence of a large background. In the case of antiprotons, the background is mostly electrons and, for experiments performed with balloons at small atmospheric depths, secondary pions and muons, both of which are produced in the interaction with the atmosphere.

To improve the detection efficiencies and identification of the desired and rejection of the unwanted particles, the CAPRICE experiment used a combination of an electromagnetic calorimeter and a newly developed Ring Imaging Cherenkov (RICH) detector with the New Mexico State University (NMSU) WiZard/CAPRICE magnetic spectrometer. In the first CAPRICE experiment, the RICH detector utilized a solid radiator of NaF, ideal for identification of antiprotons in the energy range 1–3 GeV. The CAPRICE results on positrons have been published (Barbiellini et al. 1996b). In this paper, we present the CAPRICE results on antiprotons from the 1994 experiment.

Section 2 describes the experimental apparatus, and § 3 describes the data analysis. The paper ends with a discussion in § 4.

## 2. DETECTOR SYSTEM

Figure 1 shows the NMSU-WiZard/CAPRICE spectrometer that was flown by balloon from Lynn Lake, Manitoba, Canada (56.5° N, 101.0° W), on 1994 August 8–9 at an atmospheric pressure of 3.2–4.5 mbar (altitude of 36.0–38.1 km) for 23 hr. It included, from top to bottom, a RICH detector, a time-of-flight (ToF) system, a magnet spectrometer equipped with multiwire proportional chambers (MWPC) and drift chambers (DC) and a silicon-tungsten imaging calorimeter. In the CAPRICE experiment, particular emphasis was put on particle identification. The aim was to be able to safely reject protons against positrons (Barbiellini et al. 1996b) and  $e^-$ ,  $\mu^-$ , and  $\pi^-$  against  $\bar{p}$  (this paper).

The  $50 \times 50 \text{ cm}^2$  RICH detector (Carlson et al. 1994; Barbiellini et al. 1996a), with a threshold Lorentz factor of 1.5, used a solid NaF radiator and a photosensitive MWPC with pad readout to detect the Cherenkov light image and hence measure the velocity of the particles. The time-of-flight system had two layers, with each layer made of two  $25 \times 50 \text{ cm}^2$  paddles of plastic scintillator, one above and one below the tracking stack. Each paddle was equipped with two 5 cm diameter photomultiplier tubes. The ToF system was used to give a trigger and to measure the time of flight and ionization ( $dE/dX$ ) losses of the particles. The spectrometer was equipped with a superconducting magnet and multiwire proportional chambers and drift chambers (Golden et al. 1978, 1991; Hof et al. 1994). The magnet was 61 cm in diameter and produced an inhomogeneous field of  $\sim 4 \text{ T}$  at the center of the coil operating at a current of 120 A. The spectrometer provided 19 position measurements (12 DC and seven MWPC) in the bending direction ( $x$ ) and 12 measurements (eight DC and four MWPC) in the

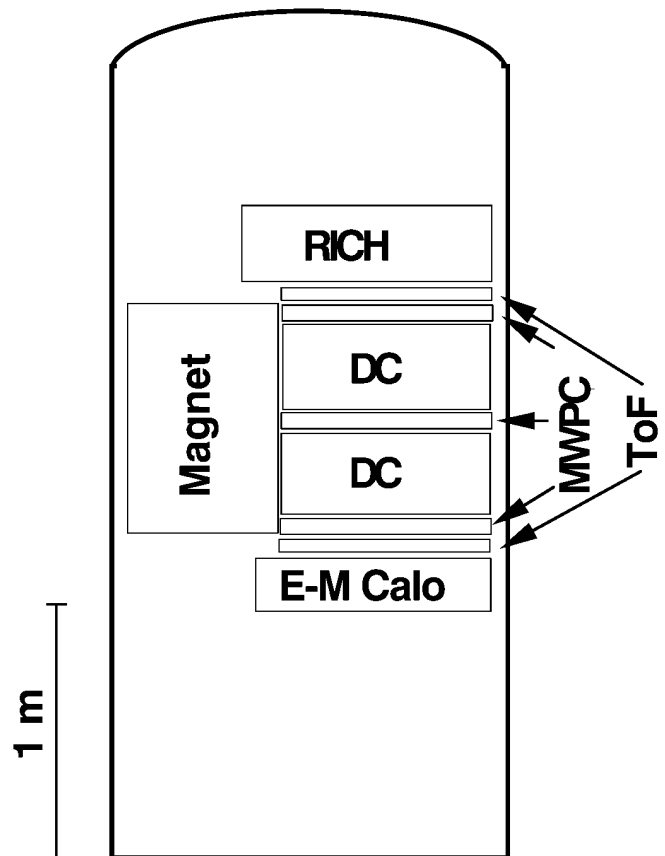


FIG. 1.—Schematic view of the CAPRICE apparatus

nonbending direction ( $y$ ). Using the position information along with the map of the magnetic field, we determined the rigidity of the particle. The average maximum detectable rigidity was 170 GV.

Finally, the electromagnetic calorimeter (Bocciolini et al. 1996) consisted of eight  $48 \times 48 \text{ cm}^2$  silicon planes, giving both  $x$ - and  $y$ -coordinate readout. Each silicon plane was interleaved with a 1 radiation length thick layer of tungsten converter. The segmentation of the silicon planes into strips provided information on the longitudinal and lateral profile of the cascade along with the total energy deposit.

## 3. DATA ANALYSIS

The analysis was based on 18 hr of data collection for a total acquisition time of 60,520 s under an average residual atmosphere of  $3.9 \text{ g cm}^{-2}$ .

The data analysis must use the information available from the different detectors to safely identify the antiprotons in a very large background of other particles. Albedo particles, as well as the large number of protons and electrons, must be rejected in the antiproton analysis. About 4% of the cosmic-ray protons interact in the atmosphere above the spectrometer and produce  $\pi^-$  and  $\mu^-$  that must be rejected. Interactions in the spectrometer and associated bar structure also result in a background of negatively charged particles. The remaining background in the antiproton sample is carefully estimated using experimental data and simulations. The selection of protons is more straightforward, with little background to reject.

Based on the ability of the RICH to identify reliably antiprotons from pions, muons, and electrons, the rigidity

range chosen for our analysis was 1.2–4.0 GV. This rigidity range was divided into two bins: 1.2–2.8 GV and 2.8–4.0 GV. At 1.2 GV, the RICH (anti)proton selection efficiency becomes higher than 50%. At a rigidity of 2.8 GV, the Cherenkov angle of (anti)protons becomes less than 6 s.d. away from the Cherenkov angle of the  $\beta$  (velocity)  $\sim 1$  particles (pions, muons, and electrons). At a rigidity of 4 GV, the (anti)proton Cherenkov angle becomes less than 3 s.d. away from the Cherenkov angle of  $\beta \sim 1$  particles.

### 3.1. Antiproton and Proton Selection

#### 3.1.1. Albedo Particles

Downgoing particles were selected using the time-of-flight information. The time-of-flight resolution of 280 ps, compared with the time of flight of more than 4 ns ensures that no contamination from albedo particles remains in the selected sample. This is verified by the RICH, where no Cherenkov light is detected for albedo particles. The RICH was capable of rejecting  $98.1\% \pm 0.5\%$  of the albedo particles that had a high enough velocity to produce Cherenkov light in the NaF radiator.

#### 3.1.2. Tracking

The tracking information must be carefully used to eliminate positively charged particles (protons) that have scattered in the tracking system and therefore look like negatively charged particles. Events with more than one track also must be eliminated. To achieve this goal, a set of conditions was imposed on the fitted tracks. These conditions represent a compromise between rejection power and efficiency and are partly based on experience gained previously using the same tracking system (Golden et al. 1991; Mitchell et al. 1996; Hof et al. 1996). They were the following:

1. At least 11 (out of 19) position measurements in the  $x$ -direction and seven (out of 12) in the  $y$ -direction were used in the fit.
2. A number proportional to the  $\chi^2$  per degree of freedom for the track fit should be  $\leq 4$  for the  $x$ -direction and  $\leq 8$  for the  $y$ -direction.
3. The estimated error on the deflection should be  $< 0.04 \text{ GV}^{-1}$ .
4. Not more than three DC layers were allowed to have additional hits at a distance larger than 4 cm from the fitted track.
5. The measured deflections using the upper and lower halves of the spectrometer should agree with those using the complete spectrometer.

Criterion 4 was introduced to reject multiple track events and criterion 5 to eliminate events in which a hard scattering had occurred. Visual inspection showed that all events rejected by criterion 4 had multiple tracks coming from above. No events with interactions in the calorimeter were rejected by this condition.

#### 3.1.3. Scintillators

Particles with a charge of 1 were selected using the measured energy loss in the top scintillator. From the observed distribution of  $dE/dX$  as a function of rigidity, singly charged proton-like events were selected in the following manner. An upper cut on  $dE/dX$  was made, which corresponds to the most probable energy loss by a proton plus

0.8 times the energy loss by a minimum ionizing particle. This criterion eliminates events where the (anti)proton was accompanied by a second particle. A lower cut was set below the most probable  $dE/dX$  for protons by 3 times the observed energy loss resolution. Multiple charged tracks produced in interactions above the tracking system were rejected by requiring that not more than one of the two paddles be hit in the top scintillator plane. We chose not to impose any conditions on the bottom scintillators to avoid losing events where an interaction in the calorimeter could produce backscattered particles that traverse the bottom scintillator paddles.

#### 3.1.4. RICH

The RICH was used to measure the Cherenkov angle of the particle and thereby its velocity. The velocity and incidence-angle-dependent Cherenkov angle resolution were determined using a large number of protons selected by the calorimeter and the scintillators. The resolution varied from 8 mrad (perpendicular incidence and  $\beta \sim 1$ ) to about 23 mrad ( $10^\circ$  off perpendicular incidence and  $\beta = 0.78$ ). Since the RICH is the only detector capable of clearly identifying antiprotons against a background of muons, pions, and electrons in the rigidity range 1.2–4 GV, strict cuts were applied on the RICH data:

1. A good agreement between the particle's impact position as determined by the RICH and the tracking system was required. The difference in  $x$  and  $y$  should be less than 3 s.d. (rigidity dependent), typically less than 5 mm.
2. Cuts on the number of pads (proportional to the number of detected Cherenkov photons) used for the reconstruction of the Cherenkov angle were also applied. More than eight pads were required in the fit.
3. Charged particles produce significantly higher signals than Cherenkov photons do in the pads. This was used to reject events with multiple charged tracks traversing the RICH, by requiring that there was only one cluster of pads with high signals.
4. The reconstructed Cherenkov angle should not deviate by more than 3 s.d. from the expected Cherenkov angle for (anti)protons.
5. To suppress the background from lighter particles, the reconstructed Cherenkov angle was required to be more than 3 s.d. (30 mrad) away from the expected Cherenkov angle for pions (the heaviest background particle).

Using these conditions, reliable Cherenkov angle information was obtained.

#### 3.1.5. Calorimeter

The calorimeter was used to identify electromagnetic showers. The longitudinal and transverse segmentation of the calorimeter combined with the measurement of the energy lost by the particle in each silicon strip resulted in high identification power ( $\sim 85\%$ ) for electromagnetic showers combined with a high rejection power ( $\sim 10^4$ ) for hadronic particles (Barbiellini et al. 1996b). In the analysis presented in this paper, the calorimeter was used to reject events with electromagnetic showers initiated by a single electron, possibly accompanied by a bremsstrahlung photon emitted in the RICH or in the dome above the detector stack (see Weber 1997 for a description of the selection criteria).

Figures 2 and 3 illustrate the calorimeter performance and show schematic views of two single events in the CAPRICE apparatus. The instrument is shown in the bending ( $x$ ) view and in the nonbending ( $y$ ) view. From top to bottom the following are displayed: the RICH seen from above, the tracking stack of multiwire proportional chambers and drift chambers, and the imaging calorimeter. Note that Figures 2 and 3 are not to scale; the calorimeter is significantly thinner than shown in the figure. Figure 2 shows a single 1.3 GV electron traversing the apparatus and emitting a bremsstrahlung photon in the RICH. The RICH shows the detected Cherenkov light image, where the ionization of the chamber gas by the electron is shown as a

cluster of pads hit in the center surrounded by the signals from the Cherenkov light. Because of total reflection in the NaF crystals, only part of the Cherenkov ring is detected. The tracking stack shows the trajectory of the electron as it is deflected by the strong magnetic field. The calorimeter shows the two electromagnetic showers produced by the electron and the bremsstrahlung photon, respectively. The origin of the bremsstrahlung photon can be located by projecting backward the direction of the shower and determining where it intersects the electron trajectory. More than  $\frac{1}{4}$  of the electrons in the rigidity region 1.2–4 GV were accompanied by a bremsstrahlung photon reconstructed in the calorimeter.

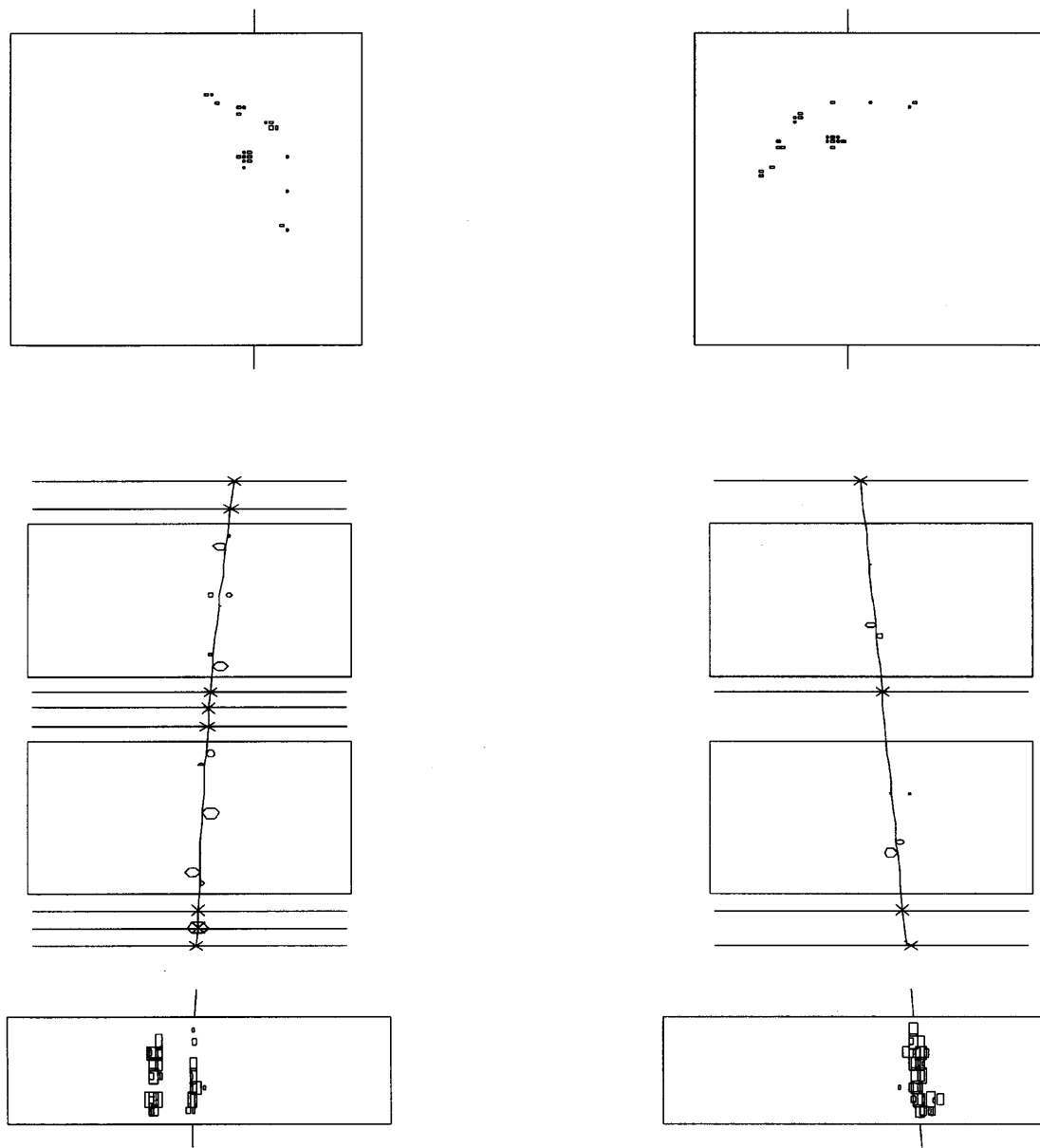


FIG. 2.—Display of a single 1.3 GV electron in the CAPRICE apparatus. The electron emits, according to an extrapolation of the track, a bremsstrahlung photon in the RICH. The instrument is shown in the bending ( $x$ ) view (*left*) and in the nonbending ( $y$ ) view (*right*). From top to bottom is displayed the RICH seen from above, the tracking stack of multiwire proportional chambers and drift chambers, with the imaging calorimeter at the bottom. Crosses indicate hits in the MWPC, and circles indicate hits in the DC with the radius proportional to the drift time. Note that the figure is not to scale. The calorimeter is significantly thinner than shown in the figure. The RICH shows the detected Cherenkov light image where the ionization of the chamber gas by the electron is shown as a cluster of pads hit in the center surrounded by the signals from the Cherenkov light. Because of total reflection in the NaF crystals, only part of the Cherenkov ring is detected. The tracking stack shows the trajectory of the electron as it is deflected by the magnetic field. The calorimeter shows the two electromagnetic showers produced by the electron and by the bremsstrahlung photon, respectively. In the nonbending view, the two showers overlap.

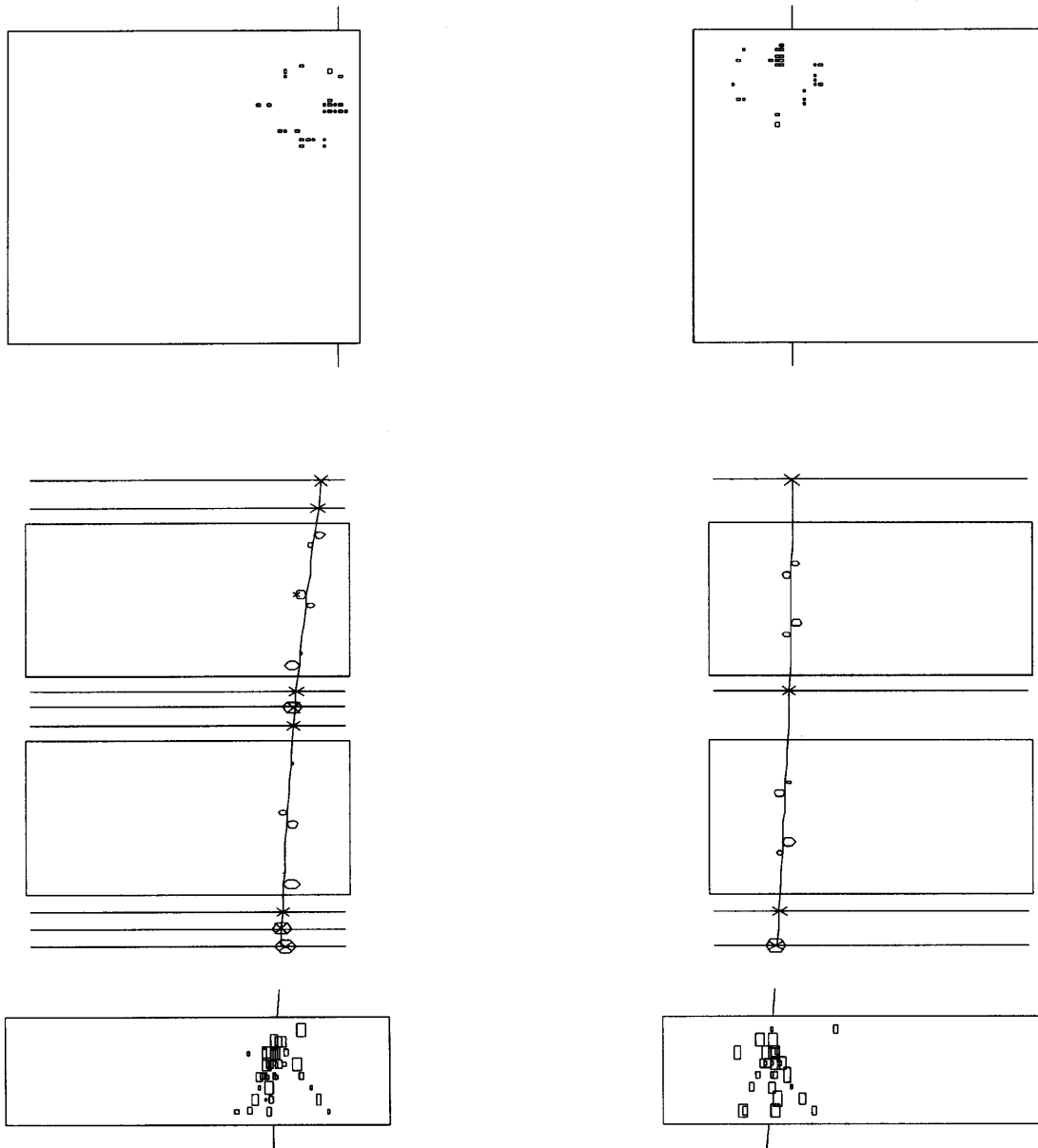


FIG. 3.—Display as in Fig. 2 of a single 2.2 GV antiproton traversing the CAPRICE apparatus. The antiproton interacts in the calorimeter, showing clearly several charged particles emerging from the vertex of interaction; this could be an annihilation in flight.

Similarly, Figure 3 shows a single 2.2 GV antiproton traversing the instrument. The ring of Cherenkov light is clearly seen in the RICH, giving an accurate velocity determination for the particle. The rigidity is measured from the deflection in the tracking system. The antiproton interacts in the calorimeter, clearly showing many charged particles emerging from the vertex of interaction; this could be an in-flight annihilation. The interaction probability for a 2.2 GV antiproton is about 40%.

#### 3.1.6. The Bar

A 17 kg, 1.2 m long aluminum bar with a 7 kg steel hook in the center, used to connect the payload to the balloon, was situated 2.3 m above the RICH. The production and loss of particles in the nonuniform I-shaped bar cannot be estimated reliably, and hence we chose to reject all particles crossing it. This was done by extrapolating the tracks to the level of the bar. This cut results in a 10% reduction of the geometrical factor.

#### 3.2. Selection Results

Nine antiprotons were found in the flight data after applying the selection criteria described above (see Table 3). Of the nine antiprotons, two (one in the first bin and one in the second) were found to have interacted in the calorimeter. This is in agreement with the simulated expectation of  $3.4 \pm 1.1$  antiproton interactions in the calorimeter. One should note that not all antiproton interactions give a detectable signal in the calorimeter.

#### 3.3. Efficiency

Whereas protons and antiprotons have very similar efficiencies in the RICH, scintillators, and the tracking system, this is not the case for the calorimeter because of the large difference in interaction properties.

A large proton sample of about 100,000 events from the flight data was used to determine the RICH, scintillator, and tracking efficiencies as a function of rigidity. Simula-

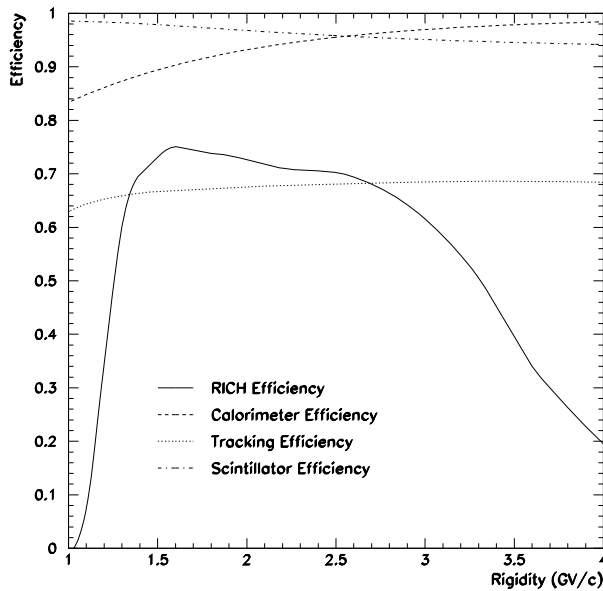


FIG. 4.—Efficiencies for the different parts of the spectrometer for detecting antiprotons. Determined from data are the efficiencies of the RICH (solid line), the tracking system (dotted line), and the scintillator  $dE/dX$  cut (dash-dotted line). The efficiency of the calorimeter antiproton cuts (dashed line) was determined by simulation.

tions were used to determine the calorimeter efficiency for antiprotons. The resulting efficiencies are shown in Figure 4 and are given in Table 1.

The scintillator efficiency was high and, as expected, only weakly dependent on the rigidity. The tracking efficiency was slightly under 70% and includes the contributions from the individual chamber efficiencies,  $\delta$ -ray production, scattering, etc.

The RICH efficiency was strongly rigidity dependent. The sharp increase with rigidity above 1 GV was due to the increasing number of Cherenkov photons emitted and hence an increased number of pads with a detectable signal. The decrease of the RICH efficiency above 2.5 GV is caused by the requirement that the Cherenkov angle should be more than 30 mrad away from the expected Cherenkov angle for pions.

The calorimeter was mainly used to reject electrons, which are the main background in the antiproton selection. The antiproton efficiency of the calorimeter was obtained from a Monte Carlo simulation based on the CERN GEANT/FLUKA-3.21 code (Brun et al. 1994). In the simulation, the full spectrometer including the magnetic field was used. The simulation results were compared with the results from beam tests of the calorimeter, and a good agreement was found (Bocciolini et al. 1993). The simulations show that the calorimeter detection efficiency for anti-

protons is rigidity dependent, as shown in Figure 4 and Table 1.

For the proton selection, the same criteria as for the antiprotons were used. The detection efficiencies are the same except for the calorimeter, which, from an experimental proton sample, selected by RICH,  $dE/dX$ , and time of flight, was found to be  $99.21\% \pm 0.03\%$  efficient and independent of rigidity.

### 3.4. Contamination

The contamination due to  $e^-$ ,  $\mu^-$ , and  $\pi^-$  in the antiproton sample was carefully studied using the two independent detectors: the RICH and the calorimeter. Simulations and experimental data taken during the flight and on the ground before the flight were used.

The calorimeter was particularly well suited to reject electrons. Detailed simulation studies showed that the shower reconstruction algorithm, designed to reject electrons while keeping as large a fraction as possible of the antiprotons, rejected 97.4% of the electrons nearly independent of rigidity in the interval 1.2–4 GV, leaving 2.6% as background. In principle, the calorimeter cuts could have a larger electron rejection power, but due to the low antiproton statistics, we chose to use calorimeter selection criteria with large efficiency even if the electron contamination is not minimized. However, the use of the RICH as the main detector to distinguish antiprotons from light particles ensures a low level of background.

The electron contamination in the RICH was studied using a sample of 1323  $e^-$  in the interval 1.2–4 GV, selected using the calorimeter and  $dE/dX$  in the scintillators. Of the 1323 events, two out of 1052 were accepted as  $\bar{p}$  in the rigidity range 1.2–2.8 GV, and two out of 271 in the rigidity range 2.8–4 GV. As expected, the RICH rejection power was rigidity dependent. The surviving fraction of electrons increased from  $0.2\% \pm 0.1\%$  between 1.2 and 2.8 GV to  $0.7\% \pm 0.5\%$  between 2.8 and 4 GV.

The combination of the calorimeter and the RICH resulted in a very small background from electrons (and interacting pions) in the antiproton sample. The electron (and interacting pion) contamination was determined by selecting all non–minimum ionizing particles in the calorimeter (1388 events, mainly  $e^-$  and a few interacting  $\pi^-$  and  $\bar{p}$ ) in the rigidity range 1.2–4 GV. A non–minimum ionizing particle is defined as a particle that deposits more energy in the calorimeter than a minimum ionizing particle (see Weber 1997). Multiplying this number by the electron rejection factors of the RICH and the calorimeter resulted in a contamination in the whole antiproton sample of less than 0.15 electrons (and interacting pions); see Table 2.

Tests in particle beams showed that muons and electrons have the same detection efficiency in the RICH. Therefore, it was assumed that the surviving fraction of muons was

TABLE 1  
ANTIPROTON SELECTION EFFICIENCIES

Rigidity at the Spectrometer (GV)	Tracking Efficiency (%)	$dE/dX$ Top Scintillator Efficiency (%)	RICH Efficiency (%)	Calorimeter Efficiency (%)
1.2–2.8	$67.6 \pm 0.4$	$96.5 \pm 0.2$	$70.2 \pm 1.0$	$93.9 \pm 0.4$
2.8–4.0	$68.6 \pm 0.5$	$94.7 \pm 0.2$	$45.3 \pm 1.0$	$97.7 \pm 0.3$

TABLE 2  
MUON AND ELECTRON CONTAMINATION

RIGIDITY AT THE SPECTROMETER (GV)	ELECTRONS		MUONS AND PIONS	
	Before RICH and Calorimeter Selection	Expected Number of Misidentified $\bar{p}$	Before RICH and Calorimeter Selection	Expected Number of Misidentified $\bar{p}$
1.2-2.8 .....	1098	$0.07 \pm 0.02$	387	$0.9 \pm 0.2$
2.8-4.0 .....	290	$0.06 \pm 0.01$	99	$0.7 \pm 0.1$

equal to the surviving fraction of electrons. This was also checked using ground data. Before the flight, long ground runs were performed where more than 400,000 events were collected. The tracking,  $dE/dX$ , and calorimeter (anti)proton selection criteria resulted in 12,819 events with negative curvature in the rigidity range 1.2-4 GV (mainly muons). The RICH (anti)proton selection criteria were applied to these events, resulting in contamination values in good agreement with the values obtained for the electrons from flight data. The surviving fraction of muons was found to be  $0.23\% \pm 0.05\%$  in the first bin and  $0.68\% \pm 0.13\%$  in the second. These numbers were used to define the contamination from the negative muons and noninteracting pions.

Defining negative muons (and noninteracting pions) as events with a minimum ionizing behavior in the calorimeter, 387 and 99 muons and pions were selected from the flight data between 1.2 and 2.8 GV and between 2.8 and 4 GV, respectively. Multiplying these numbers with the surviving fraction numbers found above, the muon/pion contamination was found to be  $0.9 \pm 0.2$  muons/pions in the first energy bin and  $0.7 \pm 0.1$  in the second bin. This contamination, and the small electron and interacting pion contamination, was later subtracted from the antiproton signal and is shown in parentheses in Table 3. It is worth noting that the calorimeter cannot separate muons and pions from noninteracting antiprotons and therefore cannot be used to further reject muons and pions.

As a cross-check, the calorimeter electron rejection criteria were applied on all negative events, leaving 433 particles (muons, pions, antiprotons, and 2.6% of the electrons) between 1.2 and 2.8 GV and 118 events between 2.8 and 4 GV. Multiplying these numbers with the RICH rejection

power determined for the ground muons results in a contamination of  $1.0 \pm 0.2$  in the first bin and  $0.8 \pm 0.2$  in the second. This is in agreement with the previous results. The background analysis results are summarized in Table 2.

3.5. Antiproton Flux and Antiproton to Proton Ratio at the Top of the Atmosphere

To obtain the antiproton flux and the antiproton to proton ratio at the top of the atmosphere, it is necessary to correct for the number of secondary particles produced and lost in the residual atmosphere and in the instrument itself. Furthermore, the detector efficiencies, geometrical factor, and total live time have to be taken into account.

The geometrical factor ( $G$ ) at different rigidities was obtained with a Monte Carlo technique (Sullivan 1971); see Table 4. The fractional dead time during the flight was  $0.7310 \pm 0.0006$ , resulting in a total live time ( $T_{live}$ ) of  $16,280 \pm 36$  s.

Since the detector efficiencies varied with rigidity, it was important to properly define the rigidity values at which these efficiencies had to be estimated. For protons, the rigidity range was split into bins of 50 MV  $c^{-1}$  width, narrow enough that the efficiencies do not vary appreciably inside each bin. For each bin, we counted the number of protons and corrected for the detector efficiency. For the antiprotons, because of the low statistics, the efficiencies were weighted with a theoretical antiproton flux (see Table 1). In this process, we used the expressions for the mean interstellar antiproton flux given by Gaisser & Schaeffer (1992), corrected for the solar modulation conditions during the CAPRICE flight. The solar modulated flux ( $flux_{mod}$ ) at an energy  $E$  is given as function of the interstellar flux ( $flux$ ) by

TABLE 3  
SUMMARY OF PROTON AND ANTIPROTON RESULTS

RIGIDITY AT THE SPECTROMETER (GV)	OBSERVED NUMBER OF EVENTS <sup>a</sup>		EXTRAPOLATED NUMBER AT TOP OF PAYLOAD		ATMOSPHERIC CORRECTION		
	$\bar{p}$	$p$	$\bar{p}$	$p$	$\bar{p}$	$p$	$\bar{p}/p$ at TOA <sup>b</sup>
1.2-2.8 .....	4(1)	124658	8.6	303433	1.5	8484	$2.5_{-1.9}^{+3.2} \times 10^{-5}$
2.8-4.0 .....	5(0.7)	25260	17.7	90451	1.4	1662	$1.9_{-1.0}^{+1.6} \times 10^{-4}$

<sup>a</sup> The numbers shown in parentheses are the estimated muon, pion, and electron background.

<sup>b</sup> TOA = top of the atmosphere. The quoted errors are a combination of statistical and systematic errors.

TABLE 4  
ANTIPROTON AND PROTON FLUXES AT THE TOP OF THE ATMOSPHERE (TOA)

Kinetic Energy at TOA (GeV)	Geometrical Factor (m <sup>2</sup> sr)	Antiproton Flux at TOA <sup>a</sup> (m <sup>2</sup> sr s GeV) <sup>-1</sup>	Proton Flux at TOA <sup>a</sup> (m <sup>2</sup> sr s GeV) <sup>-1</sup>
0.6-2.0 .....	$179.1 \pm 2.8$	$1.9_{-1.4}^{+2.4} \times 10^{-2}$	$743 \pm 17$
2.0-3.2 .....	$177.5 \pm 2.8$	$5.3_{-2.9}^{+4.5} \times 10^{-2}$	$278 \pm 10$

<sup>a</sup> The quoted errors are a combination of statistical and systematic errors.

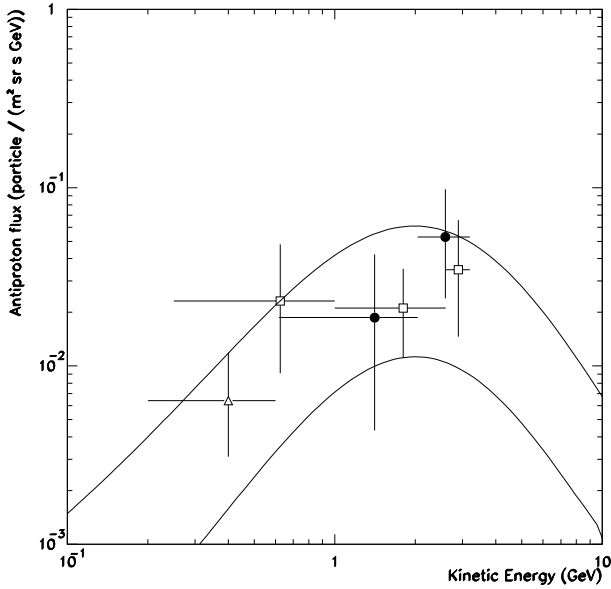


FIG. 5.—The antiproton flux at the top of the atmosphere obtained in this work and compared with other recent experiments that have published results on the antiproton flux. Data from Mitchell et al. (1996; *open box*), Moiseev et al. (1997; *open triangle*), and this work (*filled circle*). The solid lines are the maximum and minimum  $\bar{p}$  fluxes as calculated by Gaisser & Schaeffer (1992). The theoretical fluxes, but not the experimental values, were corrected for the solar conditions during the CAPRICE flight.

(Gleeson & Axford 1968)

$$\text{flux}_{\text{mod}}(E) = \frac{E^2 + 2m_0 E}{(E + Ze\Phi)^2 + 2m_0(E + Ze\Phi)} \text{flux}(E + Ze\Phi),$$

where  $E$  is the kinetic energy in MeV,  $Ze$  is the charge of the particle, and  $m_0$  is the (anti)proton rest mass. The parameter

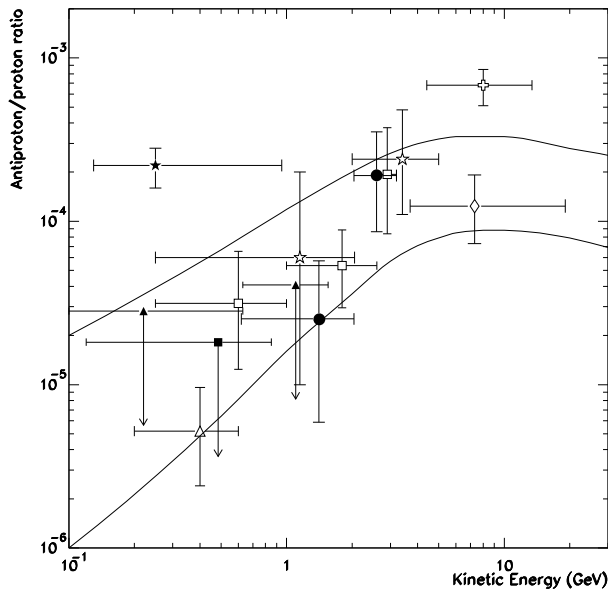


FIG. 6.—The  $\bar{p}/p$  ratios at the top of the atmosphere obtained in this work compared with previous measurements. Data from Golden et al. (1984; *open cross*), Buffington et al. (1981; *filled star*), Bogomolov et al. (1987, 1990; *open star*), Mitchell et al. (1996; *open box*), Hof et al. (1996; *open diamond*), Moiseev et al. (1997; *open triangle*), and this work (*filled circle*). Experiments reporting only upper limits are Stochaj et al. (1990; *filled square*) and Salamon et al. (1990; *filled triangle*). The solid lines are the maximum and minimum ratios as calculated by Gaisser & Schaeffer (1992).

$\Phi$  for the CAPRICE flight was found to be 500 MV using data from the neutron monitor counter CLIMAX (University of Chicago 1996) and the work by Paradis (1995).

All antiprotons and protons interacting with the payload material above the tracking system were assumed to be rejected by the selection criteria. The data were corrected for these losses with multiplicative factors, using the expression for the interaction mean free path for the different materials in the detectors given by Stephens (1997). The corrected number of antiprotons and protons at the top of the payload are given in Table 3.

The production of secondary antiprotons in the atmosphere has been studied by several authors (Pfeifer, Roesler, & Simon 1996; Stephens 1997). For the atmospheric secondary antiproton production, we used the calculation by Stephens (1997), and for that of protons, we used the data of Papini, Grimani, & Stephens (1996). The secondary produced particles were normalized with the acceptance and live time of the experiment and subtracted from the corrected numbers using a mean residual atmosphere of  $3.9 \text{ g cm}^{-2}$ . Finally, the data were corrected for losses in the atmosphere above the detector due to interactions, giving the number of antiprotons ( $N_{\bar{p}}^{\text{TOA}}$ ) and protons ( $N_p^{\text{TOA}}$ ) at the top of the atmosphere; see Table 3.

The antiproton flux is given by

$$\text{flux}(E) = \frac{1}{T_{\text{live}} G \Delta E} N_{\bar{p}}^{\text{TOA}}(E),$$

where  $\Delta E$  is the energy bin corrected to the top of the atmosphere. The resulting antiproton flux is given in Table 4. The total errors include both statistical and systematic errors. Figure 5 shows the antiproton flux at the top of the atmosphere measured by this and other recent experiments together with theoretical predictions. The theoretical antiproton limits were set by Gaisser & Schaeffer (1992), assuming that the source of interstellar antiprotons is interaction of cosmic rays with the interstellar medium. The theoretical fluxes, but not the experimental values of the other experiments, were corrected for the solar modulation conditions corresponding to the CAPRICE flight ( $\Phi$ ).

The antiproton to proton ratio was calculated from

$$R(E) = N_{\bar{p}}^{\text{TOA}}(E)/N_p^{\text{TOA}}(E)$$

and is summarized in Table 3. The ratio is also presented in Figure 6, along with the results from other balloon experiments and theoretical predictions by Gaisser & Schaeffer (1992).

#### 4. DISCUSSION

For the first time, the combination of an electromagnetic calorimeter and a ring imaging Cherenkov detector has been used to measure the cosmic-ray flux of antiprotons. This combination has made it possible to identify accurately antiprotons in the presence of a large background of lighter, negatively charge particles. It also allows an accurate determination of the contamination within the antiproton sample.

The flux of antiprotons and the ratio of antiprotons to protons increase over the kinetic energy interval 0.6–3.2 GeV. In agreement with other recent data (e.g., Mitchell et al. 1996), our findings support the conjecture that the antiprotons in this energy range are produced in the interstellar



medium by primary cosmic rays colliding with interstellar gas.

The combination of all available data on the ratio in the energy range 0.3–3 GeV (Stochaj et al. 1990; Salamon et al. 1990; Moiseev et al. 1997; Bogomolov et al. 1987, 1990; Mitchell et al. 1996; this work) shows an increase with energy in agreement with calculations by Gaisser & Schaeffer (1992). However, the combined data do not rule out a faster increase than calculated. The two measurements that have been reported above 4 GeV by Golden et al. (1984) and by the MASS91 experiment (Hof et al. 1996) differ by about 3 s.d., and further measurements are clearly needed in order to rule out any exotic antiproton production. Fortunately, new experiments are in progress.

For very low kinetic energies, below 0.5 GeV, the solar modulation affects the flux significantly. However, the existing data do not rule out contributions from, for example, dark matter particle annihilations. Calculations by Mitsui, Maki, & Orito (1996) show that in the above scenario the antiproton spectrum would flatten at lower energies; new experiments are in progress to test this scenario. A flattening at low energies could also be caused by diffuse scat-

tering on hydromagnetic waves, as shown by Simon et al. (1996).

New experimental facilities will soon become available with space borne magnetic spectrometers (e.g., Adriani et al. 1995) that will allow long exposure times and thereby give statistically improved data on the antiproton flux.

This work was supported by NASA grant NAGW-110, the Istituto Nazionale di Fisica Nucleare (INFN), Italy; the Agenzia Spaziale Italiana; DARA and DFG in Germany; EU SCIENCE; the Swedish National Space Board; and the Swedish Council for Planning and Coordination of Research. The Swedish-French group thanks the EC SCIENCE program for support. We wish to thank the National Scientific Balloon Facility (NSBF) and the NSBF launch crew that served in Lynn Lake. We would also like to acknowledge the essential support given by the CERN TA-1 group and the technical staff of New Mexico State University and of INFN. One of us (M. B.) wishes to thank the Consiglio Nazionale delle Ricerche, Italy, for a grant that partly sponsored his activity.

#### REFERENCES

- Adriani, O., et al. 1995, Proc. 24th Int. Cosmic Ray Conf. (Rome), 3, 591  
 Barbiellini, G., et al. 1996a, Nucl. Instrum. Methods, A371, 169  
 ———, 1996b, A&A, 309, L15  
 Bociolini, M., et al. 1993, Nucl. Instrum. Methods, A333, 77  
 ———, 1996, Nucl. Instrum. Methods, A370, 403  
 Bogomolov, E. A., et al. 1979, Proc. 16th Int. Cosmic Ray Conf. (Kyoto), 1, 330  
 ———, 1987, Proc. 20th Int. Cosmic Ray Conf. (Moscow), 2, 72  
 ———, 1990, Proc. 21th Int. Cosmic Ray Conf. (Adelaide), 3, 288  
 Brun, R., et al. 1994, "Detector Description and Simulation Tool," CERN program library, W5013  
 Buffington, A., Schindler, S. M., & Pennypacker, C. R. 1981, ApJ, 248, 1179  
 Carlson, P., et al. 1994, Nucl. Instrum. Methods, A349, 577  
 Gaisser, T. K., & Schaeffer, R. K. 1992, ApJ, 394, 174  
 Gleeson, L. J., & Axford, W. I. 1968, ApJ, 154, 1011  
 Golden, R. L., et al. 1978, Nucl. Instrum. Methods, 148, 179  
 ———, 1979, Phys. Rev. Lett., 43, 1264  
 ———, 1984, Astrophys. Lett., 24, 75  
 ———, 1991, Nucl. Instrum. Methods, A306, 366  
 Hof, M., et al. 1994, Nucl. Instrum. Methods, A345, 561  
 ———, 1996, ApJ, 467, L33  
 Kiraly, P., Wdowczyk, J., & Wolfendale, A. 1981, Nature, 293, 120  
 Mitchell, J., et al. 1996, Phys. Rev. Lett., 76, 3057  
 Mitsui, T., Maki, K., & Orito, S. 1996, preprint (UT-ICEPP 96-03)  
 Moiseev, A., et al. 1997, ApJ, 474, 479  
 Papini, P., Grimani, C., & Stephens, S. A. 1996, Nuovo Cimento, 19, 367  
 Paradis, P. 1996, Ph.D. thesis, New Mexico State Univ.  
 Pfeifer, Ch., Roesler, S., & Simon, M. 1996, Phys. Rev. C, 54, 2, 54  
 Rudaz, S., & Stecker, F. W. 1988, ApJ, 325, 16  
 Salamon, S., et al. 1990, ApJ, 349, 78  
 Silk, J., & Srednicki, M. 1984, Phys. Rev. Lett., 53, 624  
 Simon, M., et al. 1996, ApJ, 456, 519  
 Stecker, F. W., Protheroe, R. J., & Kazanas, D. 1981, Proc. 17th Int. Cosmic Ray Conf. (Paris), 9, 211  
 Stecker, F. W., & Wolfendale, A. W. 1984, Nature, 309, 37  
 Stephens, S. A. 1997, Astropart. Phys., 6, 229  
 Stochaj, S. J., et al. 1990, Proc. 21th Int. Cosmic Ray Conf. (Adelaide), 3, 284  
 Sullivan, J. D. 1971, Nucl. Instrum. Methods, 95, 5  
 University of Chicago. 1996, Neutron Monitor Data (National Science Foundation grant ATM 94-20790; <http://astro.uchicago.edu/home/web/pyle/neutron.html>)  
 Weber, N. 1997, Ph.D. thesis, Royal Inst. Tech., Stockholm